



# Scaling for steady and traveling shock wave/turbulent boundary layer interactions

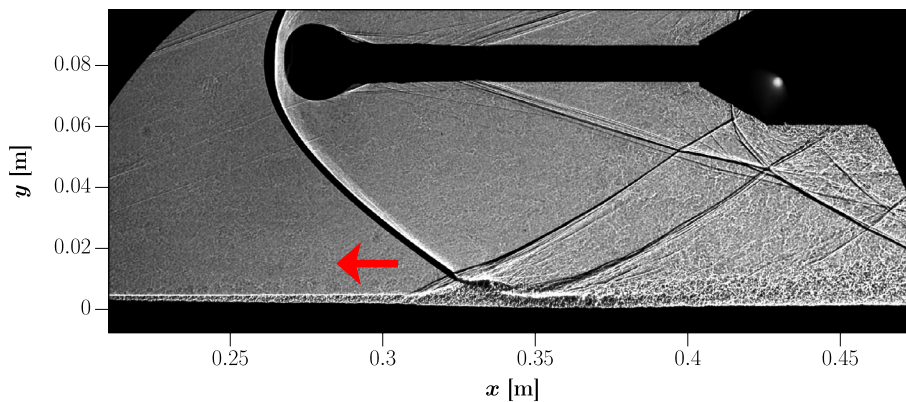
P. S. R. Touré<sup>1</sup> · E. Schülein<sup>1</sup>

Received: 6 November 2019 / Revised: 18 April 2020 / Accepted: 27 May 2020 / Published online: 20 June 2020  
© The Author(s) 2020

## Abstract

Shock-wave/boundary-layer interactions (SW–BLIs) play an important role in a wide range of transonic, supersonic and hypersonic applications. Fundamental studies on stationary interactions have been conducted extensively during the last 60 years. However, unsteady SWBLIs with traveling shock fronts have been little studied on canonical geometries. In the present experimental investigation, the influence of a uniformly moving impinging shock on the separated SWBLI flow is analyzed, with a freestream Mach number of 3 and a traveling Mach number in upstream direction of 0.5. To evaluate this effect, stationary reference SWBLIs have been investigated in a wide ranging study. A scaling method from the literature has been enhanced to drastically reduce the data scattering using a new approach accounting for the Reynolds number influence. The results gathered from the traveling interactions were within the spread of reference data, considering the true shock-wave Mach number of 3.5. The validity of the modified scaling approach to describe the interaction length in cases with steady and traveling shock-wave/turbulent-boundary-layer interactions is discussed.

## Graphic abstract



## 1 Introduction

Research on shock-wave/boundary-layer interactions has been conducted for over 60 years, and a lot of progress has been achieved (Gaitonde 2015). Still it belongs to the fundamental problems of high-speed fluid dynamics, combining key areas such as turbulence, compressibility effects and viscous–inviscid interactions (Schülein 2006). A profound understanding of SWBLI is needed for a wide range of applications in the transonic, supersonic and hypersonic flow regime. This interaction can, for example, induce buffeting

✉ P. S. R. Touré  
patrice.toure@dlr.de  
E. Schülein  
erich.schuelein@dlr.de

<sup>1</sup> Institute for Aerodynamics and Flow Technology, German Aerospace Center (DLR), Bunsenstr. 10, 37073 Göttingen, Germany

on transonic wings, inlet instability and high thermal loads at supersonic and hypersonic vehicles. To examine the fundamental relationships, the complexity of the applications is usually reduced by using canonical geometries such as 2-D compression ramps or reflected shocks on a flat plate. This approach resulted in a generally good understanding of stationary SWBLI (Babinsky and Harvey 2011). Also, the understanding of SWBLI unsteadiness due to flow separation made progress in the recent years (Clemens and Narayanaswamy 2014). However, relatively little attention was paid to investigate unsteady SWBLI with traveling shock fronts leading to flow separation and occurring, for example, in shock tubes or during ram-jet starts inside the inlet. In these cases, it is important to determine the time scales in which the flow adapts to new flow conditions. A better understanding of traveling shock fronts, which induce flow separation, can help to improve the modeling of phenomena like unstart of supersonic inlets. The authors, however, have no knowledge of fundamental research dedicated to analyze the influence of a traveling impinging shock front on a turbulent boundary layer, which results in SWBLI movement with flow separation. To isolate this effect of a traveling shock front, all other flow parameter variations should be minimized by using a test rig with a canonical geometry, enabling a shock front with constant shock strength to travel uniformly over a well-defined supersonic boundary layer.

The conducted research on stationary shock-wave/boundary-layer interactions done so far is essential to be able to evaluate the influence of a traveling impinging shock front on SWBLIs because a stationary reference is needed for comparison (Chapman and Tobak 1988). Large qualitative similarities are known between different kinds of SWBLIs with flow separation for a wide range of geometric and aerodynamic parameters as shown with the “free interaction concept” (Chapman et al. 1958). The pressure jump due to the interaction is divided into two parts. The first part called the “free interaction zone” is the compression zone in vicinity of the separation point starting at the upstream influence point named  $x_1$ , which defines the interaction onset. This region is only dependent on flow conditions at the interaction onset, not of the incident shock intensity. The incident shock strength has an influence on the second compression region which arises near reattachment, determining the extent of the separation bubble (Babinsky and Harvey 2011).

The influence of freestream Mach number and Reynolds number on SWBLI has been analyzed since 50 years (Thomke and Roshko 1969). A Mach number increase in the inflow decreases the upstream influence length as well as the length of the separation bubble (Holden 1977). The influence of the Reynolds number is more complex. In a not fully developed turbulent boundary layer, the interaction length increases with the Reynolds number until it reaches a tipping point. In the further course, the interaction length

decreases (Babinsky and Harvey 2011). Different correlations for the interaction length  $L$  exist as functions of the Reynolds number showing a change in the trend at approximately  $Re_\delta \leq 10^5$  ( $Re_\delta$  based on the boundary layer thickness  $\delta$ ) (Settles et al. 1981; Zheltovodov et al. 1993).

Spatial scaling approaches for the pressure and heat flux distributions in the interaction region use the interaction length  $L$  and the upstream influence location on the plate  $x_1$  as well as the undisturbed boundary layer thicknesses (Chapman et al. 1958; Dupont et al. 2006). Empirical correlations also exist to predict incipient separation using critical oblique shock wave strengths (Zukoski 1967). A new scaling approach for the interaction length was described by Souverein et al. (2013). The Mach number, the shock strength and the displacement thickness of the boundary layer  $\delta^*$  are acknowledged by the method.

Investigations on self-induced flow oscillations in separated flows provide conclusions that are useful for the analysis of traveling SWBLI. The SWBLI unsteadiness can be divided into high-frequency, small-scale motions characterized by the incoming boundary layer, as well as low-frequency, large-scale motions with a typical frequency range of one to two orders of magnitude lower. The pulsation of the separated flow is characteristic for the large-scale unsteadiness and goes along with a shock-foot movement across the intermittent region, found in many studies for different canonical geometries (Muck et al. 1985; Dolling 1988; Poggie and Smits 2001). The shock-foot oscillations are described by a typical Strouhal number of  $0.02 \pm 0.01$  indicating a characteristic separation shock speed  $U_s$  in the order of  $0.02\text{--}0.04 U_\infty$  (Clemens and Narayanaswamy 2014).

Studies on externally forced SWBLI unsteadiness can be divided in two main groups:

1. research on singular or cyclic angular ramp movement which forces shock intensity variation at a fixed SWBLI location;
2. research on oscillating impinging shock fronts induced by rotating or pitching shock generators mounted above the boundary layer.

The external forcing mechanism of SWBLI due to angular ramp movement has first been analyzed by Roberts (1989). The experiments were conducted with single-cycle motions at a Mach number of 6.85. The forced increase in the shock intensity resulted in an increase in the separation region at the fixed location of the ramp. However, a time delay between the ramp movement and the reaction of the induced flow was found. Park et al. (1994, 2001) conducted a detailed numerical analysis for singular and cyclic upward and downward ramp movements with varying angular velocities with Euler-flow and Navier–Stokes simulations. The single-cycle shock front was curved and after the ramp movement

stopped the steady state condition set in after an extended period of time, confirming the result of Roberts. Experiments of oscillating ramps conducted by Coon and Chapman (1995) as well as simulations performed by Park et al. (2001) at high angular ramp speeds led to a distinct hysteresis of the local wall pressure.

Studies on pitching or rotating shock generators (Bruce and Babinsky 2008; Liu and Zhang 2011; Pasquariello et al. 2015) started years after the first ramp movement experiments come closest to the canonical geometries searched for by the authors. In these studies, a shock intensity variation is accompanied by an oscillating shock-impingement location. During the interaction movement, the shock strength and the shock front velocity are time-dependent. Bruce and Babinsky (2008) generated an oscillating normal shock wave by applying a sinusoidal variation of downstream pressure at a low Mach number of 1.4. The experiments had been conducted at a parallel-walled duct, and the back-pressure variation was induced via a rotating elliptical cam. It was found that the normal shock oscillation is a mechanism to adjust its absolute Mach number (shock strength) by motion to the back-pressure change. An inviscid analytical model could describe the dynamics of the resulting unsteady shock motion for weak interactions with small separation bubbles. The extent of the interaction oscillated due to the continuously changing normal shock strength. In another approach, Pasquariello et al. (2015) conducted LES simulations and experiments of a pitching shock generator in the form of a wedge. It has been used to achieve a long traveling distance for an oblique shock, impinging on a flat plate. In approximately 15 ms the wedge pitched from  $0^\circ$  to  $17.5^\circ$ . This resulted in an incident shock movement with varying speeds and shock strengths. The fluid–structure interaction of the dynamic incident shock impinging on a flexible panel has been investigated and unsteady effects analyzed. Liu and Zhang (2011) used a pitching mechanism for an entire ramjet inlet model to analyze unstart phenomena for dynamic angle-of-attack variations. The studies using pitching or rotating shock generators resulted in an unsteady SWBLI and had not the goal to isolate the influence of the shock movement on SWBLI. Thus, a strong influence of the varying shock strength on the SWBLIs was acceptable or even desired. The resulting shock movements were oscillations which mostly occurred within a small streamwise region.

The first goal of the present study was to experimentally investigate the influence of a uniform impinging-shock movement, in upstream direction with constant shock strength, on the interaction length. The desired motions could be achieved in the present work by launching movable shock generators in upstream direction with uniform speed. To see an effect of shock movement on the interaction length, it was decided for this study to use the highest possible, well reproducible shock generator speed. The forced

movement should be faster than the characteristic movement due to inherent shock oscillations. To distinguish the shock movement effect from other key parameter influences, we had to validate and further develop the scaling laws. This was achieved using available data and a comprehensive reference data set obtained in the present work for steady SWBLI. The parameter study conducted include the variations of the shock intensity and the boundary-layer thickness for steady and traveling shock waves. The resulting interactions were visualized using the shadowgraph technique, and the shadowgrams have been evaluated to automatically detect the induced shock fronts and interaction lengths of the SWBLIs.

## 2 Experimental program

### 2.1 Wind tunnel

The wind tunnel tests were conducted in the Ludwig-Tube Facility DNW-RWG at DLR Göttingen. This facility covers a Mach number range of  $2 \leq M_\infty \leq 7$  and a unit Reynolds number range of  $2 \times 10^6 \text{ m}^{-1} \leq \text{Re}_1 \leq 11 \times 10^7 \text{ m}^{-1}$ . The specific feature of a Ludwig Tube is the usage of a long expansion tube as a pressure reservoir, which is closed at one end and has a gate valve attached to the other end, followed by a supersonic nozzle, test section and dump tank. After opening the gate valve, a shock wave propagates into the low-pressure region and expansion waves propagate into the high-pressure region (the expansion tube). The expansion waves are reflected at the closed tube end. As long as these waves do not reach the nozzle throat, test gas flows out at nearly constant stagnation conditions through the nozzle and the test section into the dump tank. The Ludwig Tube DNW-RWG has two interchangeable tubes with a length of 80 m each, resulting in a run time of about 300–350 ms. The unheated tube A is used for  $M_\infty = 2\text{--}4$  and the heated tube B for  $M_\infty = 5\text{--}7$ . The low operation costs and the good optical access make this facility best suited for optical experimental methods and heat flux measurements. In the present experiments, the unheated tube A is used. The cross section of the test section is  $0.5 \times 0.5 \text{ m}^2$ . The freestream Mach number and the unit Reynolds number remain generally constant with  $M_\infty = 3.04 \pm 0.04$  and  $\text{Re}_1 = 46 \pm 1 \times 10^6 \text{ m}^{-1}$  at  $p_0 = 0.5 \text{ MPa}$  and  $T_0 = 255 \text{ K}$ .

### 2.2 Models

A common flat plate model is used in combination with a set of shock generators to investigate stationary and movable SWBLIs. The main flat plate has a sharp leading edge (leading edge radius on the order of  $10 \mu\text{m}$ ), a length of 669 mm and a width of 400 mm, as shown in Fig. 1. The end-of-transition

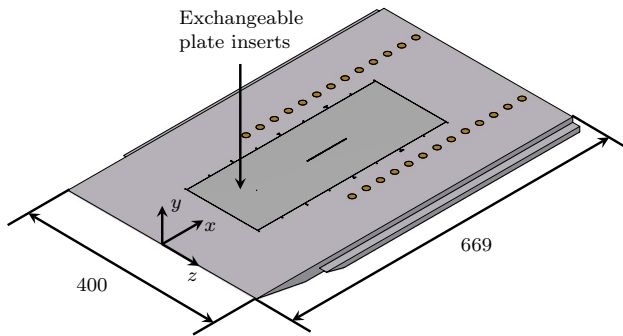


**Fig. 1** Sketch of the flat plate model

location on the flat plate is approximately at  $x = 100$  mm for the above-mentioned flow conditions (Schülein and Wagner 2015). Exchangeable plate inserts were used for the different measurement techniques. The whole test model used for the stationary SWBLI investigations is shown in Fig. 2a. Six stationary shock-generator cylinders with diameters  $d$  from 5 mm to 30 mm in 5 mm steps were used (each 245 mm in width  $W$ ). The streamwise position from the leading edge of the plate to the axis of the shock generator cylinders is adjustable from  $\Delta x = 39$  mm (Pos. A) to 339 mm (Pos. K) in 30 mm steps. The cylinder axis was alternatively located at two different vertical distances above the main plate  $\Delta y$  of 80 mm and 100 mm, enabling an additional variation of the shock impingement strength. The test model with movable shock generators used in the second part of investigations is shown in Fig. 2b. In this test series six exchangeable low weight shock generators, made of carbon fiber composites (CFC), have been used with diameters ranging from 18 mm to 28 mm in 2 mm steps, each 200 mm in width. The reduced span is

a result of weight and stability limitations. The CFC shock generators were assembled on a steel bolt and positioned at  $\Delta y = 80$  mm above the main plate. The distance  $\Delta x$  decreased during the shock generator movement.

### 2.3 Measurement techniques

The standard shadowgraph technique was used in these investigations to visualize the shock-wave/boundary-layer interaction. The recording of the shadowgrams in stationary interaction cases was made by a high-speed CMOS camera, model *pco.dimax HS4*, with a frame rate of 1 kHz at  $2000 \times 2000$  pixel. A flashlamp, model *HSPS NANO-LITE KL-L*, with a half width flash duration of 18 ns as well as a continuous light source with an exposure time of 10  $\mu$ s was used for the illumination. The interaction cases with traveling shock fronts, however, were recorded with a CMOS camera, model *Phantom v1210*, with a frame rate of 19 kHz at  $1280 \times 512$  pixel and a resolution of  $\sim 5$  px/mm. A pulsed diode laser, model *CAVILUX Smart*, was used as light source. It had a flash duration of 20 ns and a wave length of 640 nm (red light).

The pitot pressure profiles of the undisturbed flat plate boundary layer were measured using a quickly movable, miniature Pitot probe directed against the incoming flow. The full-profile boundary layer measurements, for each discrete streamwise position, were conducted during a single run of the wind tunnel. The pitot probe was vertically moved from the plate surface into the flow field for up to 9 mm, with an adjustment accuracy of 1  $\mu$ m. The traversing velocity was  $u_{\text{traveling}} = 0.053$  m/s. The Pitot pressure and static pressure signals were acquired with a sampling rate of 5 kHz. The Pitot pressure  $p_{02}$  and the wall pressure  $p_w$  were detected

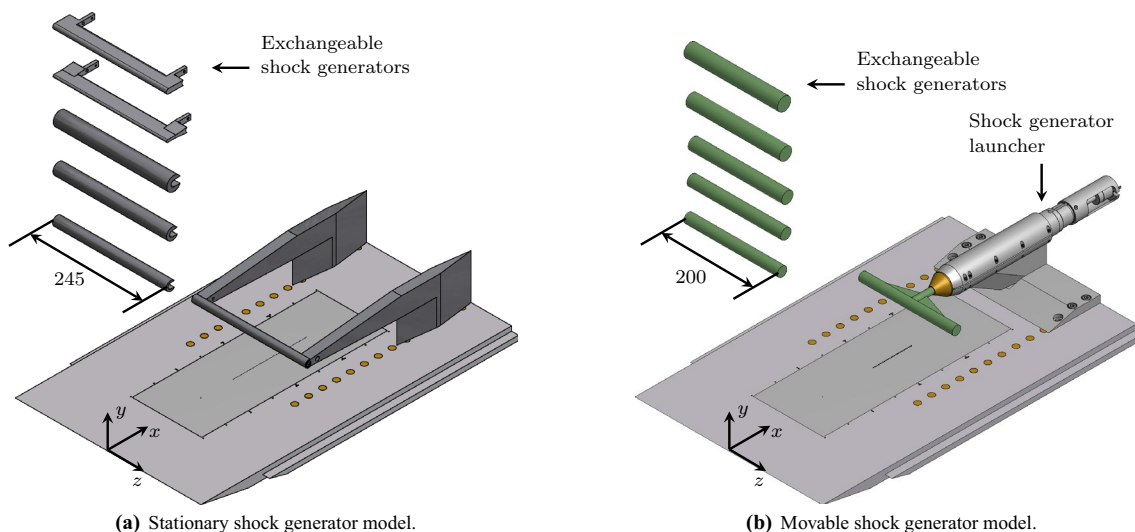


**Fig. 2** Sketch of the wind tunnel models



by fast response pressure transducers, models *Kulite XCQ-062-IBAR-A* and *Kulite XT-190M-15A*. Pitot-profile measurements have been conducted along the centerline of the flat plate at locations ranging from  $x = 153$  mm to 393 mm, in 60 mm steps. The pressure signals were processed to calculate iteratively the Mach number profiles using the Rayleigh–Pitot equation. Under the assumption of a turbulent recovery factor  $r$  of 0.89 and a constant wall temperature  $T_w$ , the Crocco–Busemann equation is used to iteratively calculate the velocity and temperature profiles using the  $M$ -profile as input. The algorithm described by Schülein et al. (1996) was used to calculate the skin friction coefficients  $c_f$  from velocity profiles. It is based on the Van Driest transformation in conjunction with the method described by Huang et al. (1993).

## 2.4 Test matrix

The measurement campaign of stationary interactions conducted to produce a reference data set comprises 53 cases (Table 3, “Appendix”). The definition of the Run ID is a short form of the used setup. For example, “G30\_100” is indicating the shock generator Position G ( $\Delta x = 219$  mm), diameter  $d$  of 30 mm and vertical spacing  $\Delta y$  of 100 mm. The nominal shock intensity  $\xi_{\text{imp}}$  is defined as the inviscid pressure ratio expected locally at the virtual impingement location in absence of the flat plate.  $\xi_{\text{imp}}$  varied from 1.82 to 3.84 in the stationary interaction data set. According to Moeckel (1949), the shape and the local intensity of the curved 2-D bow shock wave generated in front of a circular cylinder in a cross-flow is a function of the vertical distance normalized by the cylinder diameter  $\Delta y/d$ . Thus,  $\Delta y/d$ , which decreases from 16 to 3.2, characterizes  $\xi_{\text{imp}}$ .

The test matrix for the interaction cases with a moving shock-wave front is given in “Appendix” (Table 4). The moving interactions were gathered for impinging shocks traveling in upstream direction, relative to the plate, with a Mach number of  $M_{\text{trav}} \approx 0.5$ . The nominal shock intensity detected varies from  $\xi_{\text{imp}} = 3.47$  to 4.40 and is higher than comparable stationary interaction cases due to the higher resulting shock-wave Mach number of  $M_s \approx 3.5$ . The impingement position  $x_{\text{imp,move}}$  listed corresponds to the location where the moving interactions were evaluated. The positions are in the range of  $x_{\text{imp,move}} = 336$  mm  $\pm$  11 mm, because there a nearly constant speed was found for all test cases.

## 3 Methods

### 3.1 Shadowgram analysis

In this section, the method of quantitative evaluation of the experimental shadowgrams is presented. For the stationary

interaction cases, 20 consecutive short-exposure shadowgrams in each run were averaged to one final picture, which corresponds to a time span of 20 ms. The vibration-related displacements from frame to frame were corrected by fitting the model edges from each shadowgram onto the reference image taken before wind-tunnel start. In the cases with traveling interactions, no averaging was conducted and each single image was evaluated. The single images were positioned in relation to the reference image by using the stationary parts of the test section. In Fig. 3a a shadowgram of a stationary interaction case is shown as an example with the reference model edges presented as light-blue lines. For this task the edge detection function from the *GNU Octave* programming language is used. It is a multi-stage algorithm using the Canny method (Canny 1987; Adler and Hauberg 2019). The Prewitt operator was used as a filter to find the intensity gradient of the image in both horizontal and vertical direction and then to calculate the gradient direction for each pixel. The following steps of the Canny algorithm are as described in the literature. The model edges in the stationary interaction cases are used to correct a possible image shift. The positioned shadowgrams are then used to generate the averaged shadowgrams of stationary interactions for further analysis.

In the next step, the front of the impinging bow shocks in the shadowgrams was detected to get the impingement position  $x_{\text{imp}}$  on the plate. Because the separation bubbles are relatively big, the detected bow shock could not be linearly extrapolated down to the flat plate without doing a significant error. Therefore, the undisturbed bow shock contour, predicted by Reynolds-averaged Navier–Stokes simulations (RANS) in the absence of the flat plate, was used to extrapolate the detected bow shock up to the wall, as displayed by the orange line in Fig. 3a.

The last step was to detect the interaction length in the shadowgrams. Figure 3b, c shows a magnified view of the SWBLI in Fig. 3a. The impinging bow shock is again displayed as an orange line in Fig. 3c crossing the flat plate at the impinging position  $x_{\text{imp}}$ . The separation shock, detected in the shadowgram by the Canny algorithm, is displayed as the blue line. Because the separation shock detection was not possible inside the boundary layer, the method described by Elfstrom (1972) is applied to extrapolate it to the wall. The most upstream compression wave (red line) inside the boundary layer was bent toward the floor until it reached the sonic line by using the Mach number profiles, which were available from direct measurements described in Sect. 2.3. The intersection of the calculated first compression wave with the flat plate is determined as the upstream influence point  $x_1$ . By definition, the interaction length  $L$  was finally determined as the distance between  $x_1$  and  $x_{\text{imp}}$ .

The impinging shock and the separation shock were visualized in the shadowgrams with a limited thickness. By

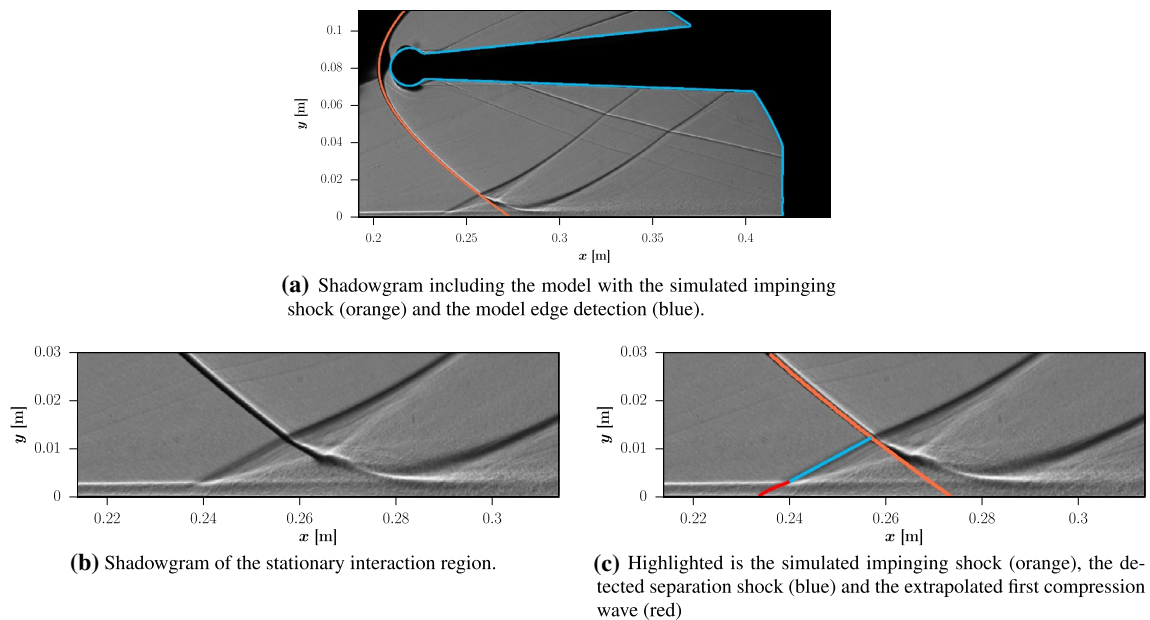


**Fig. 3** Example of the interaction length detection (case G20\_80)

using the mean position, the uncertainties can be indicated with approximately  $\pm 0.75$  mm for  $x_{\text{imp}}$  and  $x_1$  as well as with  $\pm 1.5$  mm for  $L$ . The impinging shock angle  $\beta_{\text{imp}}$  uncertainty is in the order of  $\pm 0.1^\circ$ .

### 3.2 Detailing the upstream moving impinging shock generation

The dynamic SWBLI measurements are realized by using shock generators moving at maximum test speed reached in upstream direction, as presented in Sect. 2.2. The whole movement process is filmed during the test time. Two shadowgrams are shown in Figs. 4 and 5 as an example. The stationary SWBLI before the launch is shown in Fig. 4, and a snapshot of the uniformly moving interaction is shown in Fig. 5 with a red arrow indicating the movement direction. The following components are visible in both shadowgrams:

the flat plate, the shock generator, the launcher as well as the window edges. A reproducible result is achievable when the shock generator orientation and the acceleration of the impinging shock can be predicted. In Figs. 4 and 5 the shock generator has an oval shape in the shadowgrams, partly due to optical distortion (see Fig. 3a) and partly due to a minor angular misalignment which was less than  $1^\circ$ . The small roll angle is presumed to be negligible. During the upstream movement of the shock generator, a slight deflection in  $y$ -direction can occur. This is detected and incorporated by the shadowgram analysis. The white dot visible in Fig. 5 (at  $x \approx 0.43$  m and  $y \approx 0.075$  m) is the propellant gas (hot gas) which leaves the launcher. This gas gets carried away in a flow region where it has no influence on the SWBLI under investigation.

In Fig. 6 the time history of the traveling speed of the impinging shock-wave front is shown as detected for two

**Fig. 4** Shadowgram with a movable shock generator before the launch, at a stationary position (Run ID: 2.move22)

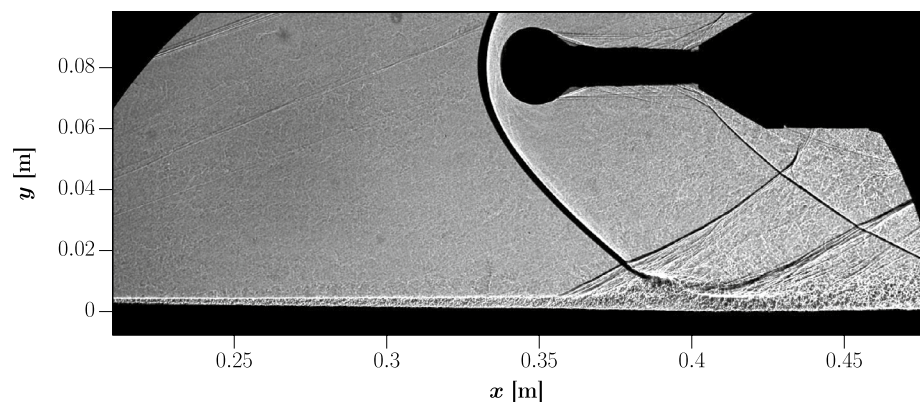


**Fig. 5** Shadowgram with a moving shock generator at uniform traveling speed (Run ID: 2.move22)

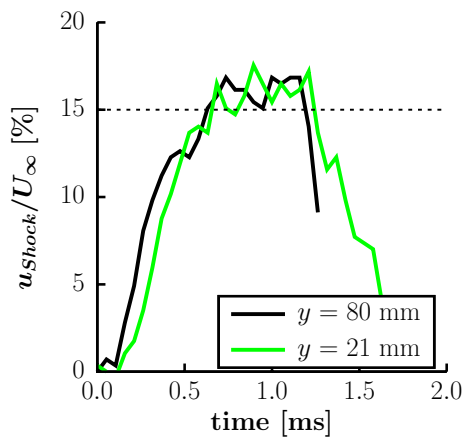
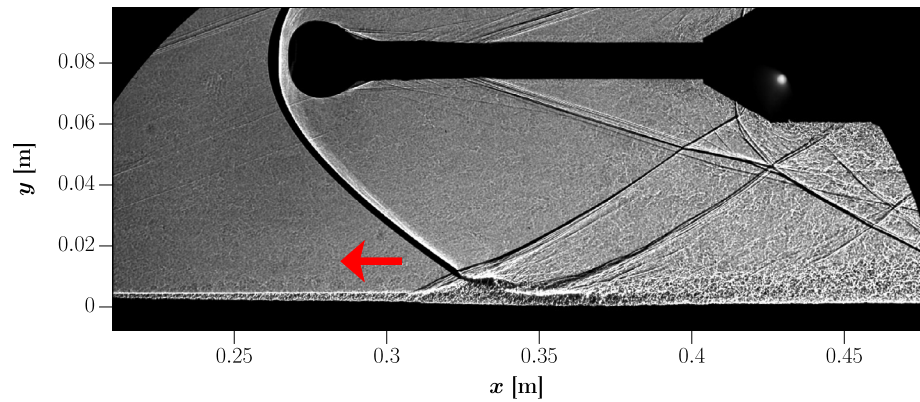


**Fig. 6** The velocity time histories of the impinging shock at the positions  $y = 21$  mm and  $y = 80$  mm (Run ID: 1.move18)

different vertical positions  $y = 21$  mm and  $y = 80$  mm. The acceleration of the impinging shock leads to a shock contour adjustment causing a phase-shifting between the time histories obtained at different distances from the shock generator axis. Right in front of the shock generator, at  $y = 80$  mm, the shock front starts to accelerate earlier than at the second position closer to the plate ( $y = 21$  mm). In both cases the traveling speed increases within about 0.7 ms until it reaches a plateau. The velocity stays approximately uniform for about 0.5 ms. The distance covered during this uniform velocity period is  $\Delta x \approx 45$  mm. Afterward, the velocity decreases very fast because the plunger inside the launcher hits a rubber buffer. The acceleration slopes in Fig. 6 are slightly different, but at both positions approximately, the same uniform velocity is detected.

The light and delicate CFC shock generators have to cope with high forces during their acceleration and deceleration. The evaluated acceleration power was of  $\approx 520$  kW and the deceleration power of  $\approx 730$  kW, due to the small time scales. A power reduction by extending the time scales was not possible, due to other model and setup constraints. A

total of six shock generators have been produced with diameters of  $d = 18$  mm to 28 mm in 2 mm steps, which could not be used more than twice for mechanical reasons.

The time histories of the traveling speed for all test cases are shown in Fig. 7, as grouped by  $d$ . The reproducibility of the impinging shock speed can be demonstrated by the four shock generators used twice ( $d = 18$ –24 mm). The results of the first experiments and the corresponding reruns are in each case similar. At the velocity plateau a maximum speed of about  $15\% U_{\infty}$  was achieved, which is much higher than the mean shock velocity occurring at the SWBLI unsteadiness ( $4\% U_{\infty}$ ).

## 4 Results and discussions

In this section, the influence of the upstream movement of the impinging shock front on SWBLI will be analyzed. At first the incoming boundary layer is characterized in Sect. 4.1. Then, the stationary interaction results from the present study are discussed in Sect. 4.2. Afterward, a modified scaling approach will be introduced in Sect. 4.3 using the data obtained in the present work and literature data. In Sect. 4.4 the dynamic results are presented and compared to the stationary results by using the modified scaling approach.

### 4.1 Flat-plate boundary layer

The undisturbed flat-plate boundary layer without shock impingement was characterized with Pitot probe profile measurements. The resulting boundary-layer parameters surveyed at five streamwise positions are presented in Table 1. The measurements confirm that the boundary layer in the examined area on the flat plate has a well-developed turbulent state. The Reynolds number  $Re_{\delta}$  and the displacement thickness  $\delta^*$  are important for following evaluations to scale the stationary and moving interactions.  $Re_{\delta}$  varies from  $1.01 \times 10^5$  to  $2.34 \times 10^5$  and  $\delta^*$  from 0.72 mm to 1.79 mm

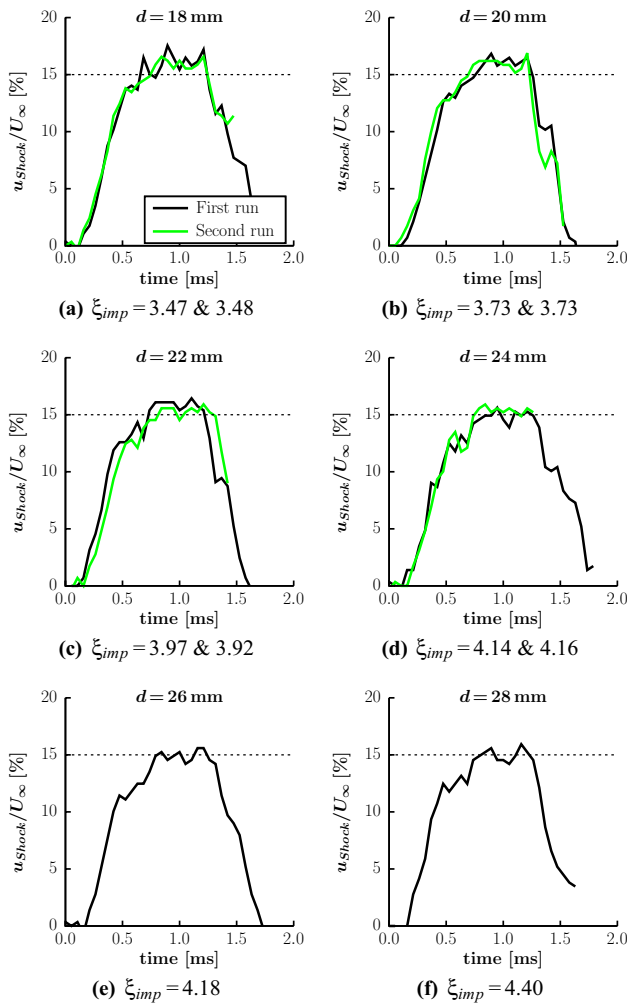


**Fig. 7** Velocity time histories of the moving impinging shocks at  $y = 21$  mm with increasing normalized shock strengths. From **a–d** the measurement reproducibility is shown

for a streamwise location ranging from  $x = 153$  mm to  $x = 393$  mm.

**4.2 Observed flow topology at steady interactions**

In this chapter shock strength and Reynolds number effects on stationary SWBLIs induced by shock generator cylinders at Mach 3 flow in the Ludwig Tube Facility are

**Table 1** Boundary layer conditions at varying streamwise positions

Experiment	$x$ (mm)	$\delta$ (mm)	$\delta^*$ (mm)	$\theta$ (mm)	$Re_1$ ( $m^{-1}$ )	$Re_\delta$ ( $10^5$ )	$c_f$	$P_0$ (bar)	$T_0$ (K)
Pitot1	153	2.18	0.72	0.14	46.2	1.01	0.00178	5.37	272.9
Pitot2	213	2.99	1.06	0.19	46.0	1.37	0.00160	4.98	260.5
Pitot3	273	3.69	1.30	0.24	46.3	1.71	0.00151	5.02	260.7
Pitot4	333	4.34	1.49	0.28	45.6	1.98	0.00148	5.34	274.3
Pitot5	393	5.07	1.79	0.33	46.2	2.34	0.00141	5.06	262.6

presented. Non-fully spanning shock generator cylinders with different diameters and moderate degrees of slenderness were rigidly mounted at their axis above the flat plate. All investigated shock generators induced boundary-layer separation on the flat plate. Since we did not use aerodynamic fences, the separation bubbles were practically open on the sides.

A typical separation bubble footprint on the flat plate is shown in Fig. 8 (Run ID: H15\_100). It was obtained using the oil film interferometry technique, explained in detail in Schülein (2006). The separation bubble is located between the separation line  $S$  and the reattachment line  $R$ . The visualized wall streamlines inside the separation bubble show that the reverse flow contains a lateral component, which increases with the distance to the centerline. This as well as the arc-like shape of the separation line is indicating that the present flow is strictly speaking not two-dimensional. Therefore, we need a special scaling law as a reference for the forthcoming considerations of traveling SWBLI.

Some typical shadowgrams of interactions with variable shock strength are shown in Fig. 9. The nominal impinging shock intensity increases here in four steps from  $\xi_{imp} = 2.36$  to 3.76. The test cases reveal separation bubbles on the flat plate, accompanied by formation of a separation shock and a reattachment shock. Upstream of the separation bubble the boundary layer edge is visible as a white stripe. The separation bubbles are always visible on the background of the undisturbed boundary layer, still existing near the side edges of the flat plate. The evaluation of shadowgrams only concerned the flow topology and the extension of the separation bubble in the area of the centerline. The results of quantitative evaluation of the shadowgrams are summarized in Table 3. Due to the increase in interaction strength, the detected interaction length  $L$  increases from 19.2 mm in Fig. 9a to 48.0 mm in Fig. 9d.

In Fig. 10 shadowgrams of SWBLI are shown with varying Reynolds numbers from  $Re_\delta = 1.30$  to  $2.54 \times 10^5$  for a constant nominal shock strength  $\xi_{imp}$  of 2.57. The figure shows the effect of the boundary layer thickness on the interaction length, because  $Re_\delta$  increases simply by increasing the boundary layer thickness. With increasing  $Re_\delta$  the interaction length  $L$  increases, from 22.0 mm in Fig. 10a to 31.9 mm in Fig. 10d (see Table 3).



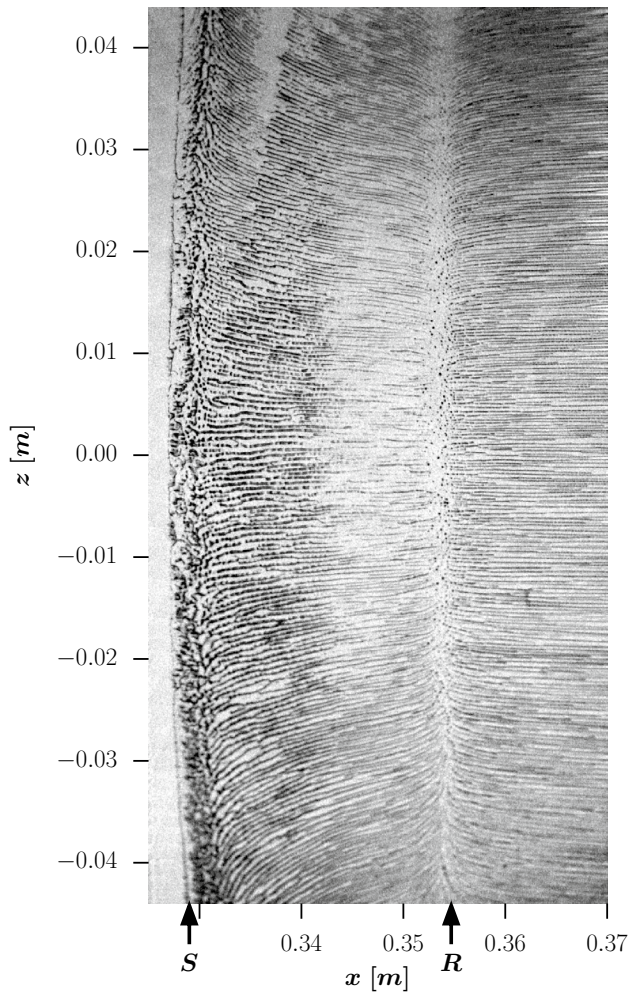


**Fig. 8** Flow separation topology showing the lateral flow component within the separation bubble. Visualization using the oil film interferometry technique. (Run ID: H15\_100)

### 4.3 Modified interaction length scaling

The original scaling approach described by Souverein et al. (2013) accounts for Mach number, shock-strength and boundary-layer effects on the interaction length. The interaction length  $L$  is defined as the distance between the upstream influence point  $x_1$  and the inviscid shock location (impingement point or kink of the ramp). The cited approach describes the scaled interaction length  $L^*$  as a function of the scaled interaction strength  $S^*$ , which are defined as:

$$S^* = kc_p = \frac{2k}{\gamma} \frac{p_{out} - 1}{p_{in} M^2} \tag{1}$$

$$L^* = \frac{L \sin(\beta)\sin(\varphi)}{\delta^* \sin(\beta - \varphi)} \tag{2}$$

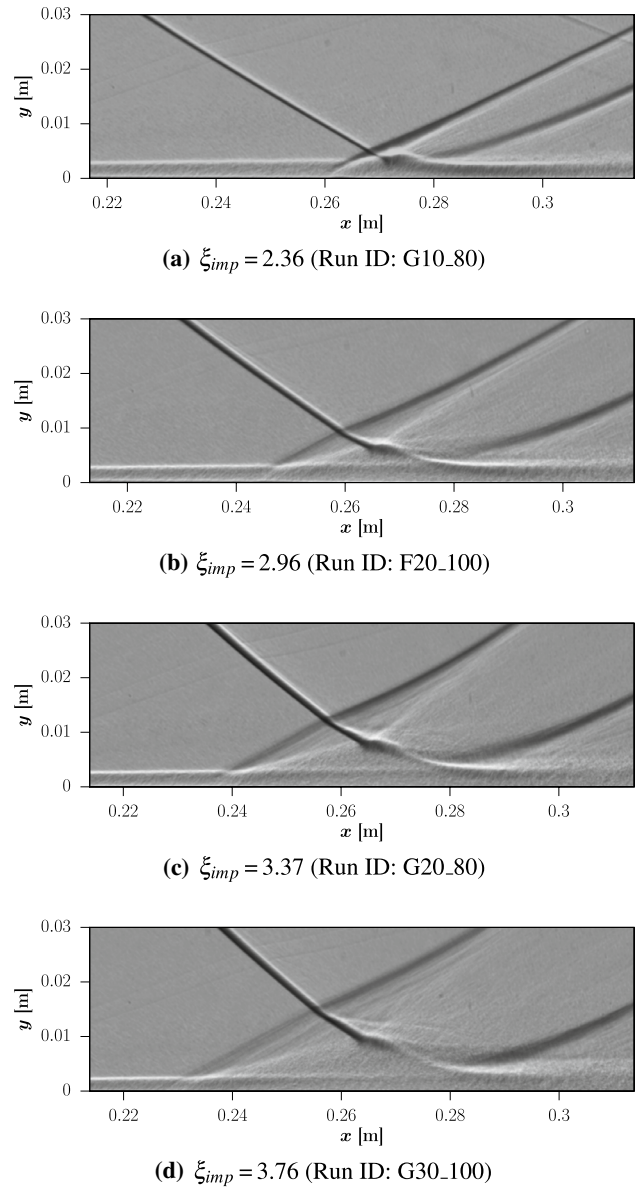


**Fig. 9** Shadowgrams of SWBLI with increasing impinging shock strength

$c_p$  is the pressure coefficient downstream of the reflected shock and  $k$  is chosen to obtain  $S^*$  of approximately 1 at the onset of separation.  $k$  is a constant function (step function) having two pieces only ( $k = 3$  for  $Re_\theta \leq 10^4$  and  $k = 2.5$  for  $Re_\theta > 10^4$ ). The interaction length  $L$  is scaled with the deflection angle of the shock  $\varphi$ , the shock angle  $\beta$  and the displacement thickness  $\delta^*$ .

To verify the scaling approach for a high Reynolds number range, the approved experimental data set of Settles et al. (1976) for two-dimensional, stationary SWBLIs induced by a ramp is used in addition to the present data set obtained in the quasi-steady case. By focusing on these two large data sets, physical causes of data scattering such as

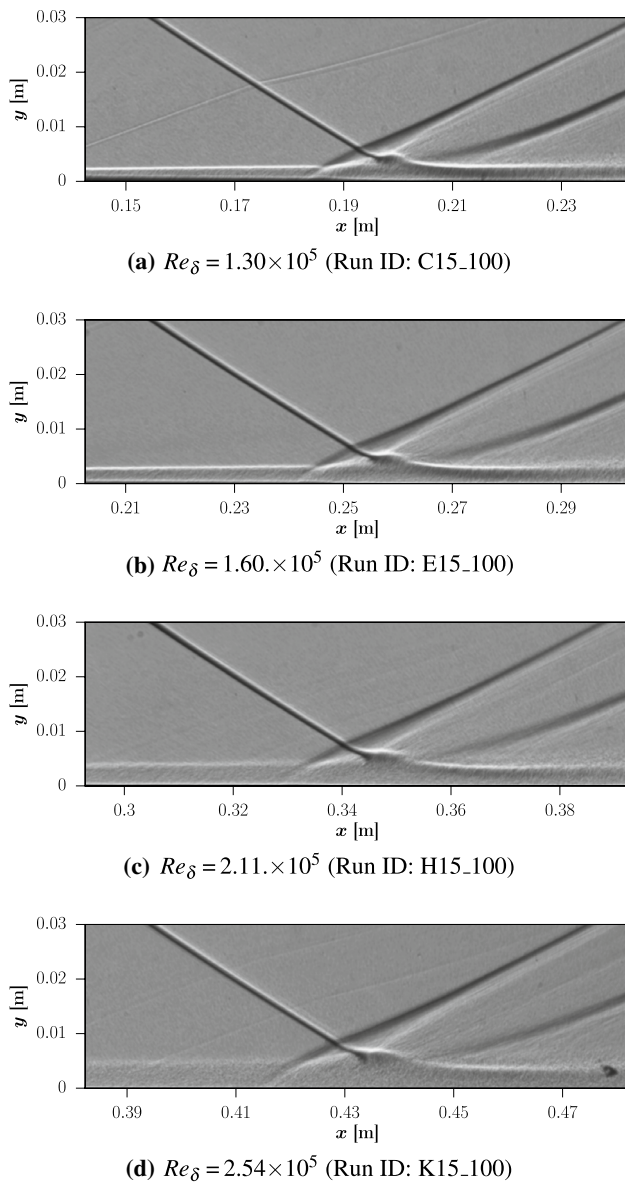
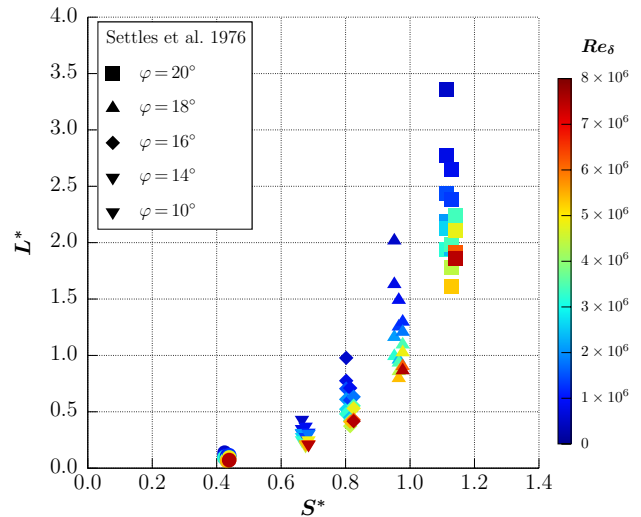


Fig. 10 Shadowgrams of SWBLI with increasing Reynolds number

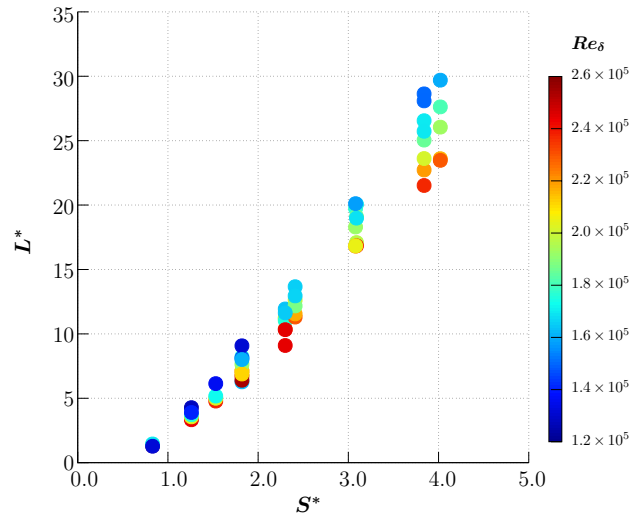
differences in test facilities, experimental setups or measurement techniques, which are not taken into account in the scaling method, could be reduced to a minimum, as will be demonstrated later in this paper.

In Fig. 11a the data by Settles et al. are scaled in accordance with the original approach from Souverein et al. (2013). The Reynolds number values are in the range of  $5.2 \times 10^5 \leq Re_\delta \leq 7.5 \times 10^6$  ( $8.1 \times 10^3 \leq Re_\theta \leq 3.1 \times 10^5$ ), given by the corresponding colorbar.

In Fig. 11b the results of the present study are scaled according to Souverein et al. (2013), but with a fixed factor  $k = 2.5$  in  $S^*$ . The ranges of the scaled interaction strengths is  $0.83 \leq S^* \leq 4.02$  and of the scaled interaction lengths



(a) Data from Settles et al. (1976).



(b) Steady shock wave data from the present study.

Fig. 11 Scaling according to Souverein et al. (2013): a original approach, b with a fixed factor  $k = 2.5$

is  $1.28 \leq L^* \leq 29.70$ . The Reynolds number values are in the range of  $1.27 \times 10^5 \leq Re_\delta \leq 2.5 \times 10^5$  ( $8.1 \times 10^3 \leq Re_\theta \leq 1.7 \times 10^4$ ), indicated by the corresponding colorbar.

In its original form  $c_p$  has been calculated considering a plane shock with the oblique shock theory based on the Mach number and the deflection angle  $\varphi$  at the boundary layer edge. For the impinging non-planar bow shock in the current setup, however, the deflection angle expected at the boundary layer edge differs from the one expected in the plane of the flat plate. Thus, to calculate  $c_p$  the deflection angle  $\varphi$  at the virtual bow shock position at the flat-plate surface (impingement point) has been used. In accordance with the oblique-shock theory for inviscid

flow all impinging shock strengths were weak enough to be reflected without a Mach-stem. However, the far-reaching results come close to this upper limit for an inviscid shock reflection at  $\beta_{\text{imp}} = 39.52^\circ$  for  $M = 3$ , corresponding to  $S^* = 5$  for  $k = 2.5$ . The interaction length  $L$  is measured by using shadowgrams as mentioned above.

The high scattering of the measurement values appearing in both cases in Fig. 11 for any roughly constant interaction strength  $S^*$  indicates a clear stratification by the Reynolds number. As mentioned above, the influence of the Reynolds number was nominally considered in the original scaling approach by the step function  $k$ . The data presented in Fig. 11 clearly show that a step function is inadequate and only a continuous function can describe the influence of the Reynolds number. Thus, a correction is required.

To improve this, we propose to introduce a new correlation function  $K$  instead of the step function  $k$ , which describes the complex influence of the Reynolds number in the wide range of shock intensities. In order to plausibly eliminate the existing Reynolds-number stratification of the validation data, the heuristic trial-and-error approach was applied to find a suitable form for  $K$ . As a result, the following form of the correlation has proven to be particularly useful:

$$K = (\text{Re}_\delta / \text{Re}_{\text{ref}})^{a \times (c_p^b)} \tag{3}$$

The reference Reynolds number  $\text{Re}_{\text{ref}}$  must be here in the range of a well-developed turbulent boundary layer, and we have decided to use  $\text{Re}_{\text{ref}} = 2 \times 10^5$  for further analysis. The constants  $a$  and  $b$  are the appropriate fitting parameters of this correlation to be found. To avoid confusion with the original scaling approach of Souverein et al. (2013), we introduce finally the normalized pressure coefficient  $c_p^* = K(\text{Re}, c_p) \times c_p$  instead of  $S^* = k \times c_p$ . This results in the modified scaling approach:

$$L^* = f(\text{Re}_\delta, c_p) = f(c_p^*) \tag{4}$$

with

$$c_p^* = K(\text{Re}, c_p) \times c_p = \left( \frac{\text{Re}_\delta}{\text{Re}_{\text{ref}}} \right)^{a \times (c_p^b)} \times c_p. \tag{5}$$

In contrast to the basic scaling approach, where  $k$  plays the role of a critical pressure coefficient corresponding to incipient separation, in the modified approach, the incipient separation does not play a special role in predicting the size of the interaction length.

Using the method of least squares, we look for the appropriate parameters  $a$  and  $b$  in  $K(\text{Re}, c_p)$  in order to approximate the combined experimental data of Settles et al. (1976) and of the present study in the best possible way. The search

revealed the optimal parameter combination with  $a = -0.27$  and  $b = 1.41$ :

$$c_p^* = \left( \frac{\text{Re}_\delta}{2 \times 10^5} \right)^{-0.27 \times (c_p)^{1.41}} \times c_p \tag{6}$$

Figure 12a shows the data of Fig. 11a, scaled using the found correlation function  $K(\text{Re}, c_p)$ . The resulting  $c_p^*$  range yields to  $0.13 \leq c_p^* \leq 1.82$ . By using the modified scaling approach the best-fit approximation found, for the data of Settles et al. (1976) (Fig. 12a, dashed line), is described by the polynomial:

$$L^* = -3.4 \times (c_p^*)^2 + 142.33 \times (c_p^*)^4. \tag{7}$$

In Fig. 12b the data from the present study are shown applying the modified scaling approach. For these SWBLIs the influence of three-dimensionality cannot be neglected, as shown in the last chapter. Therefore, a different best-fit approximation for the scaled interaction length results, was found in this case (Fig. 12b, dashed line):

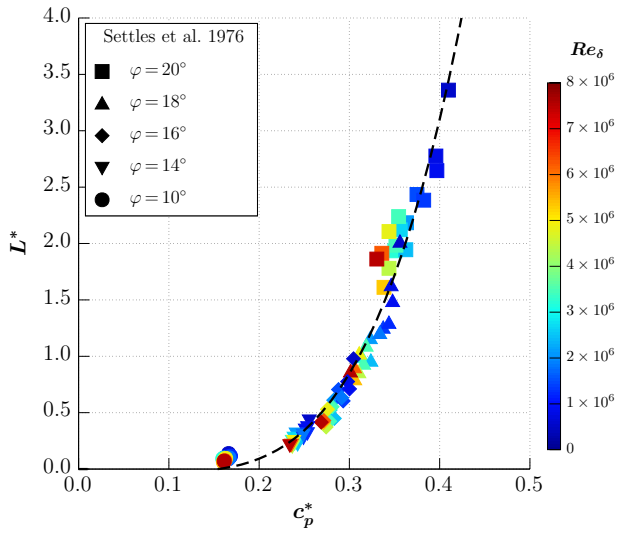
$$L^* = -1.14 \times c_p^* + 19.16 \times (c_p^*)^2 - 5.36 \times (c_p^*)^3. \tag{8}$$

The modified scaling approach reduces the data scattering of both data sets significantly. The resulting stratification of the measured values  $L^*$  by the Reynolds number is negligible in both cases. The best-fit correlation (Eq. 8) describes the experimental data with a coefficient of determination  $R^2$  (from 0 to 1) of 0.99.

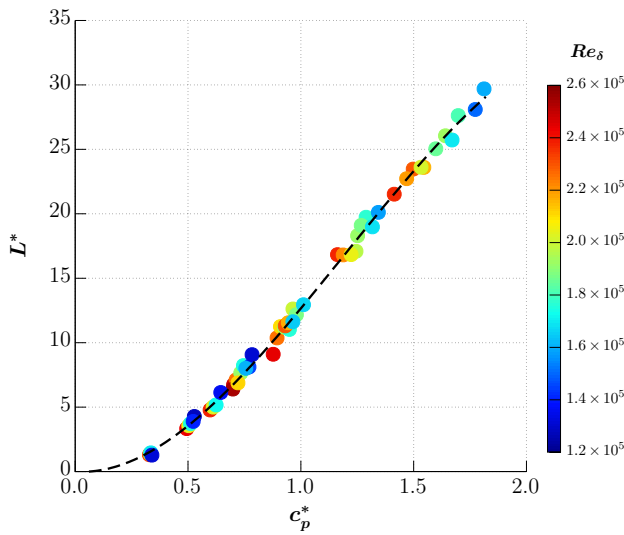
An alternative representation of the same data is shown in Fig. 13. It explicitly shows the dependence of the interaction length  $L^*$  on the Reynolds number  $\text{Re}_\delta$ . In Fig. 13a the data of Settles et al. (1976) for different ramp angles ( $c_p$  values) are presented. The measurement points are shown as symbols. The solid lines shown for five different  $c_p$  values from  $c_p = 0.173$  to  $0.451$  ( $\varphi = 10^\circ$  to  $20^\circ$  in sector 2) were calculated using Eqs. 6 and 7. The good agreement confirms that the Reynolds number influence is adequately reflected in the proposed approach. The data scattering around the lines for each nominal  $c_p$  value is partly due to a slight decrease in Mach number along the test section (from sector 1 to 3) reported by Settles et al. (1976), which leads to an increase of the experimental value of  $c_p$  at constant ramp angle. Figure 12b shows in a similar way the results of the current study for a selection of shock intensities. The results obtained using Eqs. 6 and 8 (solid lines) correlate very well with the corresponding experimental data (symbols).

Figure 14a shows a wide range of 2-D SWBLI data from different institutions scaled according to the cited approach of Souverein et al. (2013). All investigations considered are highlighted in Table 2, with the corresponding symbols. The data collection is largely based on the selection of Souverein et al.





(a) Data from Settles et al. (1976).

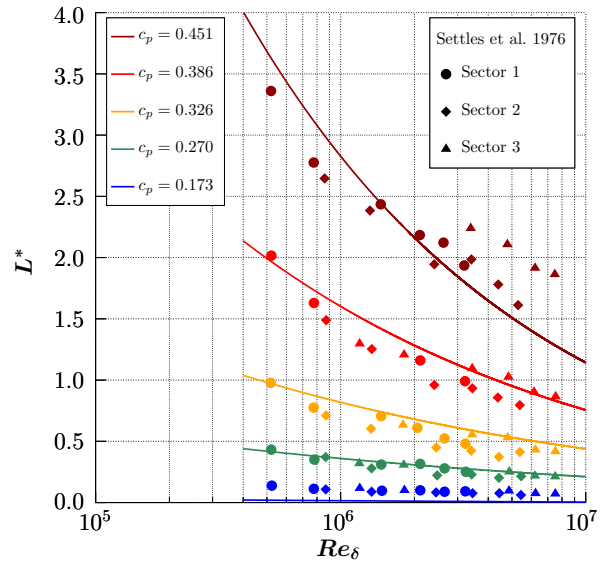


(b) Steady shock wave data from the present study.

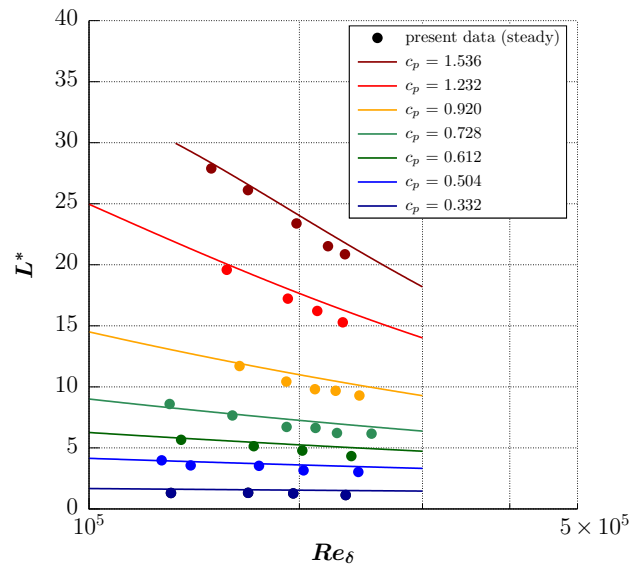
**Fig. 12** Scaling based on the modified approach (Eq. 6). Lines are corresponding best-fit approximations (Eqs. 7 and 8)

(2013). However, only part of these data was used in the present plot because the authors do not know all the required parameters in each of the original data sets. In this presentation, the current data (“+” symbol) seem to continue the trend of the data from the literature well. The scattering of the current data due to the Reynolds number variation does not seem to be particularly noticeable compared to the scattering of the remaining data.

Figure 14b shows the same data again using the proposed modified scaling approach according to Eq. 6. It is remarkable that although this scaling approach leads to a significant reduction of the scatter within each individual data set, the common course of the data breaks up into at least two individual courses. On the one hand, the data describing the incident shock



(a) Data from Settles et al. (1976).



(b) Steady shock wave data from the present study.

**Fig. 13** Reynolds number influence on the scaled interaction length. Validation of the modified scaling method

interaction (see Table 2) remain together very well, thus confirming the trend found in the current data. On the other hand, the data obtained at compression ramps form another group that looks less homogeneous but still follows its own trend. Additional parameter effects seem to appear which might have been hidden before inside the scattering, such as wall temperature effects, effects from fences and more. It can be concluded that the modified scaling approach provides a reliable basis for the representation of the own stationary data of incident shock interactions. On this basis, the effect of the moving shock fronts on the extent of the interaction area can be analyzed well in a further step.



**Table 2** Data collection considered in Fig. 14

Institute	Literature	$Re_\delta$	$M$	Symbol
<i>Compression ramps</i>				
NA <sup>a</sup>	Thomke and Roshko (1969)	$1.87\text{--}7.88 \times 10^6$	$3 \leq M \leq 5$	$\diamond$
UP <sup>b,1</sup>	Settles et al. (1976)	$0.52\text{--}7.54 \times 10^6$	2.9	$\times$
UP <sup>b,2</sup>	Dolling and Or (1985)	$1.43 \times 10^6$	2.9	$\square$
UP <sup>b,2</sup>	Selig et al. (1989)	$1.69 \times 10^6$	2.9	$\square$
UI <sup>c</sup>	Kuntz et al. (1987)	$0.31 \times 10^6$	2.9	$\circ$
<i>Incident shock reflection</i>				
TUD <sup>d</sup>	Humble (2009)	$0.61 \times 10^6$	2.1	$\nabla$
IUSTI <sup>e</sup>	Piponnier (2009)	$5.3 \times 10^6$	2.3	$\nabla$
IUSTI <sup>e</sup>	Souverain (2010)	$0.06\text{--}0.62 \times 10^6$	2.3	$\nabla$
	Present study	$0.12\text{--}0.26 \times 10^6$	3	$+$

<sup>a</sup>NASA-Ames Research Center

<sup>b</sup>University of Princeton

<sup>c</sup>University of Illinois

<sup>d</sup>Delft University of Technology

<sup>e</sup>Institut Universitaire des Systèmes Thermiques Industriels, Marseille

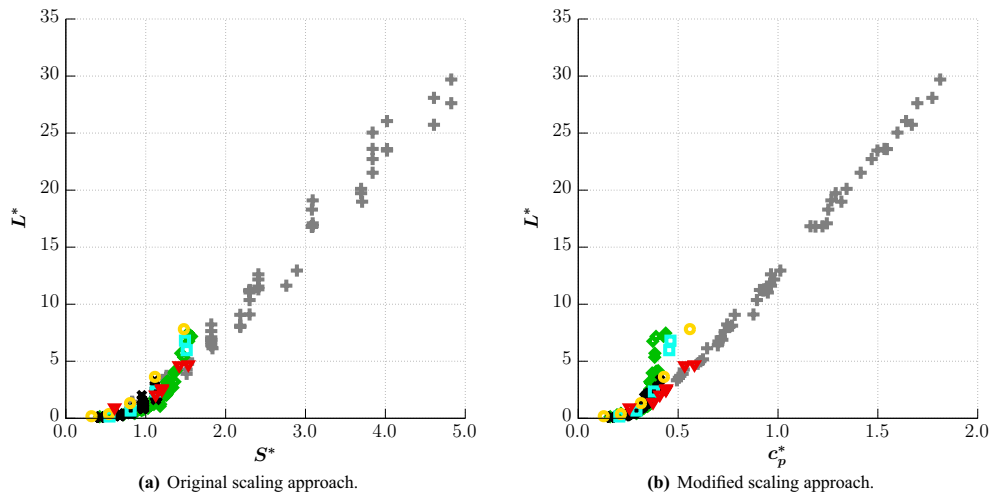


**Fig. 14** Scaling of the interaction length, with symbols as in Table 2

### 4.4 Influence of a moving impinging shock on SWBLI

In this chapter, the influence of a uniformly moving impinging shock on the shock-wave/boundary-layer interaction flow is analyzed. The turbulent boundary layer on the flat plate develops as in the stationary measurements. The traveling SWBLI on the flat plate was induced by a movable, cylindrical shock generator. The impinging shock front moving upstream induces in all cases a separation bubble on the plate which follows the shock front movement. In the present study, a traveling Mach number of  $M_{trav} \approx 0.5$  was investigated.

For each interaction strength, a shadowgram taken before the shock generator launch is shown on the left-hand side of

Fig. 15, and a shadowgram taken during the uniform traveling speed is shown on its right hand side. The impinging shock angle (thus, the local shock strength) changes with the shock generator velocity. Because the shock-wave Mach number changes from  $M_s = 3$  to  $M_s = M_\infty + M_{trav} \approx 3.5$ , the impinging shock angle decreases although the impinging shock strength increases. The interaction length  $L$  of the moving SWBLI, is for all cases smaller than the one of the stationary interaction. This is partly due to the thinning of the boundary layer with decreasing x-coordinate, and partly due to stronger compressibility effects in the interaction zone (higher Mach number). In Table 4 the quantitative results for each pair of shadowgrams shown in Fig. 15, evaluated as described in Sect. 4.3, are presented.

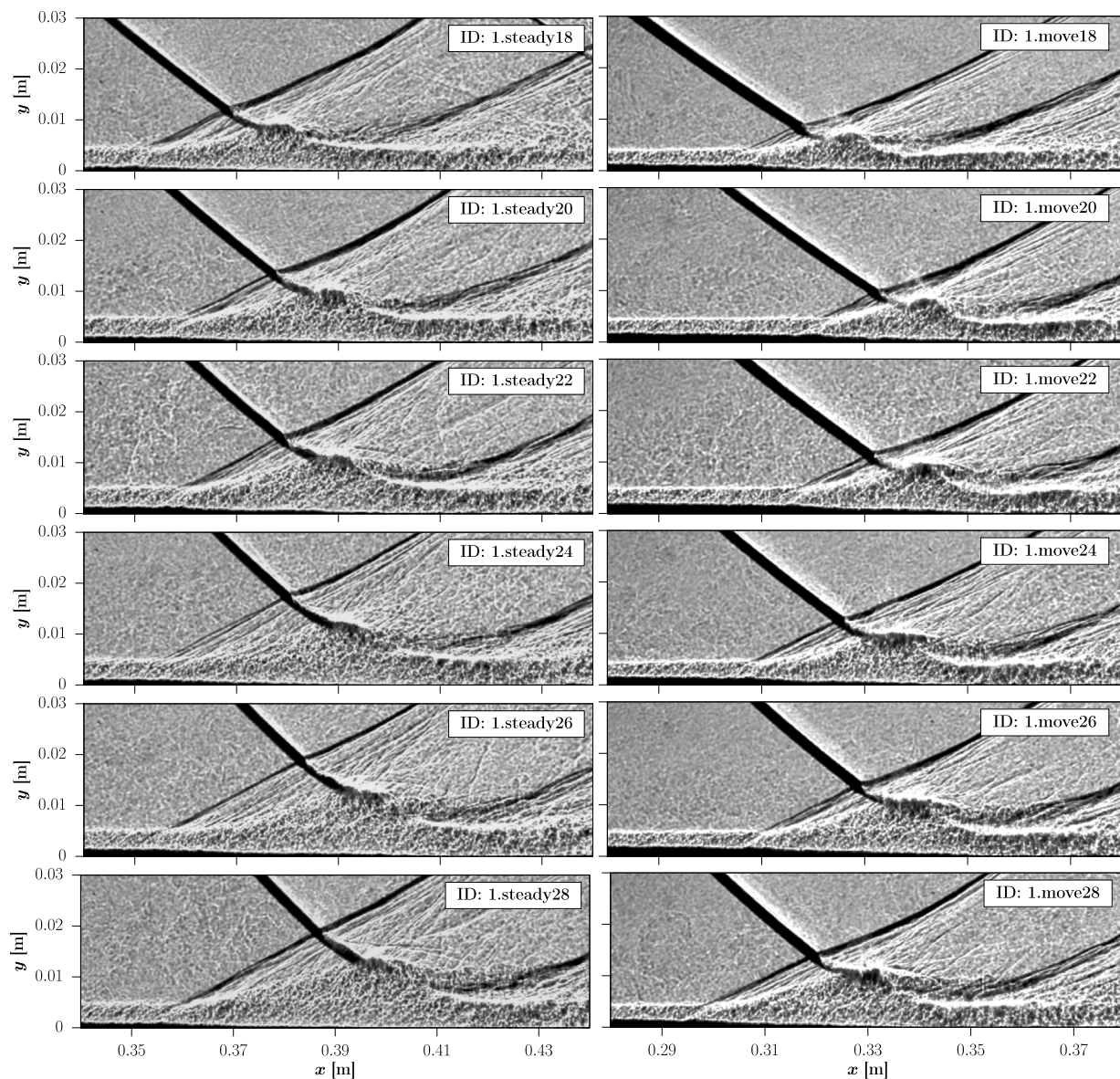


**Fig. 15** Shadowgrams of quasi-steady (left) and moving (right) SWBLI using the movable shock generators

The dynamic shock boundary layer interactions for upstream moving impinging shocks with a traveling Mach number of  $M_{\text{trav}} \approx 0.5$  can be quantitatively compared to the stationary interactions by using the modified scaling law proposed in previous chapters. In Fig. 16 the results obtained at the state before the shock generator launch are shown as green dots. The reference data used to obtain the modified scaling law in Sect. 4.3 are shown additionally as black dots. The green and the black dots together describe the stationary situation and show as expected very good agreement. The difference in span of the cylinder models (245/200 mm), is thus negligible for the scaled results.

The results of the uniformly moving interactions are shown by red dots following the same trend line as the stationary results. The best-fit correlation (Eq. 8) describes these

experimental data with a coefficient of determination  $R^2$  of 0.93 with a maximum deviation of  $\Delta L^* = 1.8$ . Thus, the scattering of data is higher in this case but still comparable to the scattering of the stationary interactions with values of  $R^2 = 0.99$  and a maximum deviation of  $\Delta L^* = 0.8$ . The reproducibility of the scaling results has been analyzed with four shock generators. The discrepancy of the non-dimensional interaction length  $L^*$  for the three shock generators with diameters  $d$  of 18 mm, 20 mm and 22 mm, which were used twice, is below  $\Delta L^* = 1.25$ . A higher discrepancy exists for the shock generator with  $d = 24$  mm only, between the experiment and the rerun, of  $\Delta L^* = 2.5$ . Therefore, it can be stated that in the investigated shock speed range (up to  $\approx 15\%$  freestream velocity) the scaled interaction length can be predicted by the scaling law found for

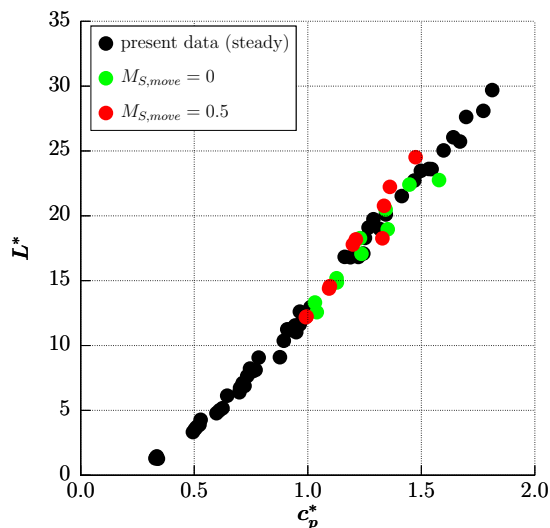


**Fig. 16** Influence of the traveling impinging shock fronts, listed in Table 4, on the interaction length scaled using the modified approach adjusted for steady flows (see Eq. 6)

stationary SWBLIs. Thus, the resulting non-dimensional interaction length is dependent on the displacement thickness of the boundary layer, the impinging shock strength and the impinging shock angle resulting from the shock-wave Mach number  $M_s$ .

## 5 Conclusion

The scalability of the interactions induced by impinging shock waves traveling over the turbulent boundary layer with nearly constant shock strengths has been experimentally studied using the shadowgraph technique. In a broad-based study, stationary reference SWBLIs were examined to evaluate the effect of shock movement. The most significant findings of the study may be summarized as follows:

1. A special experimental setup was developed to investigate the static and dynamic SWBLI under similar conditions. The impinging shock fronts induced a flow separation on the flat plate in all investigated cases. The resulting flow is strictly speaking not two-dimensional, because the separation line has an arc-like shape and the reverse flow contained a lateral flow component. Another aspect was that the SWBLIs were so strong that they were outside the limits of known scaling laws. Therefore, a special scaling law as a reference for the considerations of traveling SWBLI was needed.
2. A modified scaling approach for the interaction length  $L$  was proposed, which is based on the method described by Souverein et al. (2013). This modification considering the Reynolds number impact was successfully validated with the data available for two-dimensional,

steady SWBLI from the literature and own data from the present study. Using this method the corresponding correlation function  $K(Re, c_p)$  could be determined.

3. By applying the enhanced scaling approach, a significant reduction in data scatter could be observed for all available data sets compared to the original approach. Due to this improvement, it was immediately apparent that the common course of the data actually breaks up into at least two individual progressions. One formed for incident shock interactions and the other formed for data obtained at compression ramps that is less homogeneous. Due to the lower scattering, additional parameter effects seem to appear which might have been hidden before (temperature effects, etc.).
4. Available data from incident shock interactions were shown to be in very good agreement with data obtained in the present work. These data coincided to a very reliable and systematic dependence, which could be well approximated applying scaling law in the entire shock intensity range investigated. The resulting very low scatter of the stationary reference SWBLIs was a crucial prerequisite for the analysis of the influence of a moving impinging shock.
5. This reference scaling law was used to analyze the impact of the moving impinging shocks on the non-dimensional interaction lengths. The results obtained with moving shock fronts were within the scattering range of the reference steady-state data, but only if the true shock wave Mach number of 3.5 was taken into account. It can be concluded, that below the investigated traveling speed of  $\approx 15\%$  freestream velocity the interaction length of the traveling SWBLI can be predicted by applying the found scaling law, valid for stationary flows.

**Acknowledgements** Open Access funding provided by Projekt DEAL. The authors gratefully acknowledge the support by the anonymous reviewers of this manuscript.

**Open Access** This article is licensed under a Creative Commons Attribution 4.0 International License, which permits use, sharing, adaptation, distribution and reproduction in any medium or format, as long as you give appropriate credit to the original author(s) and the source, provide a link to the Creative Commons licence, and indicate if changes were made. The images or other third party material in this article are included in the article's Creative Commons licence, unless indicated otherwise in a credit line to the material. If material is not included in the article's Creative Commons licence and your intended use is not permitted by statutory regulation or exceeds the permitted use, you will need to obtain permission directly from the copyright holder. To view a copy of this licence, visit <http://creativecommons.org/licenses/by/4.0/>.

## Appendix

See Tables 3, 4.

**Table 3** Test matrix of the stationary shadowgram analysis

$\xi_{\text{imp}}$	$c_p$	Run ID	$d$ (mm)	$\Delta x$ (mm)	$\Delta y$ (mm)	$P_0$ (bar)	$T_0$ (K)	$Re_1$ ( $10^6$ )	$\delta$ (mm)	$\delta^*$ (mm)	$x_{\text{imp}}$ (mm)	$\beta_{\text{imp}}$ ( $^\circ$ )	$c_p^*$	$L$ (mm)	$L^*$
1.821	0.332	D5_80	5	84	80	5.03	264.4	45.41	2.88	1.00	208.4	25.8	0.340	6.2	1.28
1.821	0.332	F5_80	5	144	80	5.03	258.7	46.97	3.60	1.25	268.2	25.8	0.335	8.9	1.45
1.821	0.332	H5_80	5	204	80	4.99	263.4	45.31	4.33	1.52	329.4	25.8	0.332	10.1	1.38
1.821	0.332	J5_80	5	264	80	4.99	259.9	46.28	5.03	1.77	388.9	25.8	0.329	11.2	1.30
2.157	0.504	C10_100	10	64	100	5.03	258.5	47.07	2.70	0.93	192.8	28.1	0.528	13.5	4.28
2.157	0.504	D10_100	10	94	100	5.05	263.7	45.75	3.06	1.06	222.7	28.1	0.523	14.0	3.90
2.157	0.504	F10_100	10	154	100	5.04	261.2	46.34	3.78	1.32	283.5	28.1	0.511	16.6	3.72
2.157	0.504	H10_100	10	214	100	5.02	265.1	45.10	4.50	1.58	343.7	28.1	0.503	19.1	3.56
2.157	0.504	J10_100	10	274	100	5.02	259.6	46.61	5.21	1.83	403.7	28.1	0.494	20.8	3.33
2.359	0.612	E10_80	10	124	80	4.98	262.9	45.38	2.98	1.03	216.8	29.4	0.645	18.2	6.14
2.359	0.612	G10_80	10	184	80	5.04	260.8	46.52	3.70	1.29	276.8	29.4	0.625	19.2	5.17
2.359	0.612	I10_80	10	244	80	4.99	262.0	45.73	4.42	1.55	337.0	29.4	0.611	22.3	5.00
2.359	0.612	K10_80	10	304	80	5.01	260.5	46.32	5.12	1.80	396.5	29.4	0.598	24.8	4.78
2.565	0.728	C15_100	15	99	100	5.04	261.3	46.34	2.81	0.97	202.5	30.7	0.784	22.0	9.07
2.565	0.728	D15_100	15	129	100	5.30	272.4	45.73	3.16	1.09	231.3	30.7	0.770	22.2	8.12
2.565	0.728	E15_100	15	159	100	5.03	264.3	45.44	3.53	1.23	262.6	30.7	0.756	24.5	8.01
2.565	0.728	F15_100	15	189	100	4.88	261.4	44.86	3.88	1.36	292.3	30.7	0.746	27.8	8.23
2.565	0.728	G15_100	15	219	100	5.06	266.5	45.15	4.24	1.48	322.2	30.7	0.734	28.3	7.65
2.565	0.728	H15_100	15	249	100	5.04	263.4	45.82	4.60	1.62	352.8	30.7	0.721	27.7	6.88
2.565	0.728	I15_100	15	279	100	5.33	274.2	45.52	4.95	1.74	382.0	30.7	0.713	30.9	7.10
2.565	0.728	J15_100	15	309	100	4.90	255.9	46.55	5.31	1.87	412.5	30.7	0.702	31.5	6.74
2.565	0.728	K15_100	15	339	100	5.03	266.9	44.75	5.67	2.00	442.3	30.7	0.699	31.9	6.40
2.890	0.920	F15_80	15	189	80	5.03	258.8	46.95	3.50	1.22	259.9	32.7	0.965	29.3	11.63
2.890	0.920	G15_80	15	219	80	4.88	257.7	45.84	3.83	1.34	287.7	32.7	0.949	30.5	11.03
2.890	0.920	H15_80	15	249	80	5.05	263.2	45.93	4.21	1.47	319.9	32.7	0.927	34.2	11.19
2.890	0.920	I15_80	15	279	80	5.07	263.9	45.93	4.57	1.60	349.7	32.7	0.910	37.3	11.25
2.890	0.920	J15_80	15	309	80	5.30	272.7	45.65	4.93	1.73	379.8	32.7	0.895	37.2	10.37
2.890	0.920	K15_80	15	339	80	4.99	260.3	46.15	5.28	1.86	409.7	32.7	0.877	35.1	9.10
2.960	0.964	F20_100	20	189	100	5.02	264.6	45.32	3.65	1.27	273.1	33.1	1.012	33.0	12.95
2.960	0.964	G20_100	20	219	100	5.23	266.3	46.72	4.01	1.40	302.7	33.1	0.980	34.1	12.17
2.960	0.964	H20_100	20	249	100	5.05	264.3	45.63	4.36	1.53	332.6	33.1	0.965	38.6	12.62
2.960	0.964	I20_100	20	279	100	5.34	273.1	45.89	4.72	1.66	362.6	33.1	0.944	38.3	11.55
2.960	0.964	J20_100	20	309	100	5.10	268.0	45.12	5.08	1.79	392.9	33.1	0.931	40.4	11.30
3.367	1.232	F25_100	25	189	100	5.06	265.7	45.37	3.47	1.21	257.5	35.5	1.344	40.6	20.11
3.367	1.232	G25_100	25	219	100	5.15	265.7	46.17	3.82	1.33	287.1	35.5	1.289	44.1	19.73
3.367	1.232	H25_100	25	249	100	5.10	265.2	45.84	4.18	1.46	317.0	35.5	1.252	44.8	18.30



Table 3 (continued)

$\xi_{imp}$	$c_p$	Run ID	$d$ (mm)	$\Delta x$ (mm)	$\Delta y$ (mm)	$P_0$ (bar)	$T_0$ (K)	$Re_1$ ( $10^6$ )	$\delta$ (mm)	$\delta^*$ (mm)	$x_{imp}$ (mm)	$\beta_{imp}$ ( $^\circ$ )	$c_p^*$	$L$ (mm)	$L^*$
3.367	1.232	I25_100	25	279	100	5.04	266.3	45.03	4.53	1.59	346.9	35.5	1.223	44.8	16.83
3.367	1.232	J25_100	25	309	100	5.22	271.7	45.22	4.89	1.72	377.0	35.5	1.188	48.4	16.81
3.374	1.236	G20_80	20	219	80	4.99	261.8	45.81	3.66	1.28	273.8	35.5	1.317	40.5	18.99
3.374	1.236	H20_80	20	249	80	5.22	267.3	46.36	4.03	1.41	304.2	35.5	1.268	44.9	19.10
3.374	1.236	I20_80	20	279	80	5.08	268.8	44.74	4.39	1.54	334.5	35.5	1.245	43.9	17.09
3.374	1.236	K20_80	20	339	80	5.04	260.9	46.46	5.09	1.79	394.0	35.5	1.163	50.4	16.84
3.764	1.536	F30_100	30	189	100	5.03	265.3	45.19	3.31	1.15	244.2	37.7	1.773	47.1	28.09
3.764	1.536	G30_100	30	219	100	4.97	259.9	46.08	3.66	1.28	273.8	37.7	1.670	48.0	25.73
3.764	1.536	H30_100	30	249	100	5.11	265.6	45.83	4.03	1.41	304.4	37.7	1.598	51.5	25.04
3.764	1.536	I30_100	30	279	100	5.15	267.3	45.73	4.39	1.54	334.9	37.7	1.533	53.1	23.61
3.764	1.536	J30_100	30	309	100	5.35	272.5	46.12	4.74	1.67	364.6	37.7	1.469	55.3	22.72
3.764	1.536	K30_100	30	339	100	5.25	268.4	46.34	5.10	1.80	394.7	37.7	1.414	56.4	21.52
3.842	1.608	G25_80	25	219	80	4.89	259.6	45.44	3.51	1.22	260.9	38.2	1.812	51.7	29.70
3.842	1.608	H25_80	25	249	80	4.96	257.5	46.68	3.87	1.35	290.9	38.2	1.697	53.2	27.62
3.842	1.608	I25_80	25	279	80	5.22	270.4	45.56	4.22	1.48	320.9	38.2	1.641	54.9	26.05
3.842	1.608	J25_80	25	309	80	5.04	259.5	46.87	4.60	1.62	352.6	38.2	1.545	54.3	23.60
3.842	1.608	K25_80	25	339	80	5.07	262.3	46.36	4.93	1.74	380.6	38.2	1.498	58.1	23.47

Shock generator width = 245 mm

**Table 4** Test matrix for the SWBLIs with a uniform traveling speed  $M_{\text{trav}}$ , see Fig. 15

$\xi_{\text{imp}}$	$c_p$	Run ID	$d$ (mm)	$\Delta y$ (mm)	$P_0$ (bar)	$T_0$ (K)	$Re_1$ ( $10^6$ )	$M_s$	$\delta$ (mm)	$\delta^*$ (mm)	$x_{\text{imp}}$ (mm)	$\beta_{\text{imp}}$ ( $^\circ$ )	$c_p^*$	$L$ (mm)	$L^*$
3.14	1.080	1.steady18	18	80	4.58	244.4	46.74	3	4.99	1.76	385.4	34.1	1.032	43.0	13.31
3.47	0.996	1.move18	18	80	4.58	244.4	46.74	3.46	4.35	1.52	331.2	30.7	0.992	31.6	12.19
3.15	1.084	2.steady18	18	80	4.70	250.9	46.05	3	4.99	1.75	384.8	34.2	1.040	40.4	12.57
3.48	0.990	2.move18	18	80	4.70	250.9	46.05	3.47	4.27	1.50	325.1	30.6	0.995	31.3	12.23
3.32	1.199	1.steady20	20	80	4.58	244.8	46.61	3	5.11	1.80	395.6	35.2	1.128	45.7	14.87
3.73	1.113	1.move20	20	80	4.58	244.8	46.61	3.47	4.53	1.59	347.0	31.8	1.094	35.8	14.39
3.31	1.191	2.steady20	20	80	4.71	251.6	45.89	3	5.12	1.80	396.1	35.1	1.127	46.9	15.19
3.73	1.104	2.move20	20	80	4.71	251.6	45.89	3.48	4.44	1.56	339.4	31.7	1.097	35.8	14.57
3.49	1.319	1.steady22	22	80	4.52	245.9	45.72	3	5.15	1.81	398.3	36.2	1.237	49.5	17.07
3.97	1.228	1.move22	22	80	4.52	245.9	45.72	3.48	4.54	1.59	347.7	32.8	1.212	42.2	18.18
3.49	1.320	2.steady22	22	80	4.70	249.6	46.37	3	5.15	1.81	398.8	36.2	1.230	53.0	18.28
3.92	1.212	2.move22	22	80	4.70	249.6	46.37	3.47	4.45	1.56	339.9	32.6	1.199	40.8	17.79
3.65	1.440	1.steady24	24	80	4.53	248.2	45.07	3	5.18	1.82	401.2	37.1	1.343	56.6	20.49
4.14	1.342	1.move24	24	80	4.53	248.2	45.07	3.46	4.49	1.57	343.0	33.7	1.336	44.8	20.77
3.66	1.453	2.steady24	24	80	4.59	249.9	45.26	3	5.17	1.82	400.5	37.2	1.352	52.0	18.96
4.16	1.342	2.move24	24	80	4.59	249.9	45.26	3.47	4.53	1.59	346.5	33.7	1.329	39.7	18.27
3.83	1.600	1.steady26	26	80	4.68	249.0	46.38	3	5.22	1.84	404.5	38.1	1.448	58.9	22.41
4.18	1.391	1.move26	26	80	4.68	249.0	46.38	3.44	4.54	1.59	347.2	34.1	1.361	47.2	22.23
3.99	1.771	1.steady28	28	80	4.65	249.2	46.03	3	5.26	1.85	407.6	39.0	1.578	57.6	22.75
4.40	1.488	1.move28	28	80	4.65	249.2	46.03	3.46	4.43	1.55	338.1	34.9	1.475	48.6	24.52

Shock generator width = 200 mm

## References

- Adler A, Hauberg S (2019) The canny-algorithm source code. Retrieved July 15, 2019. <https://sourceforge.net/p/octave/image/ci/release-2.4.1/tree/inst/edge.m>
- Babinsky H, Harvey JK (2011) Shock wave–boundary-layer interactions. Cambridge University Press, Cambridge
- Bruce P, Babinsky H (2008) Unsteady shock wave dynamics. *J Fluid Mech* 603:463–473
- Canny J (1987) A computational approach to edge detection. In: Readings in computer vision. Elsevier, pp 184–203
- Chapman GT, Tobak M (1988) Bifurcations in unsteady aerodynamics—implications for testing. NASA TM 100083
- Chapman DR, Kuehn DM, Larson HK (1958) Investigation of separated flows in supersonic and subsonic streams with emphasis on the effect of transition. NACA TN 3869
- Clemens NT, Narayanaswamy V (2014) Low-frequency unsteadiness of shock wave/turbulent boundary layer interactions. *Annu Rev Fluid Mech* 46:469–492
- Coon MD, Chapman GT (1995) Experimental study of flow separation on an oscillating flap at mach 2.4. *AIAA J* 33(2):282–288
- Dolling D (1988) Unsteady shock-induced turbulent separation in Mach 5 cylinder interactions. In: 26th Aerospace sciences meeting, p 305
- Dolling DS, Or CT (1985) Unsteadiness of the shock wave structure in attached and separated compression ramp flows. *Exp Fluids* 3(1):24–32
- Dupont P, Haddad C, Debieve J (2006) Space and time organization in a shock-induced separated boundary layer. *J Fluid Mech* 559:255–277
- Elfstrom G (1972) Turbulent hypersonic flow at a wedge-compression corner. *J Fluid Mech* 53(1):113–127
- Gaitonde DV (2015) Progress in shock wave/boundary layer interactions. *Prog Aerosp Sci* 72:80–99
- Holden M (1977) Shock wave-turbulent boundary layer interaction in hypersonic flow. In: 15th Aerospace sciences meeting, p 45
- Huang P, Bradshaw P, Coakley T (1993) Skin friction and velocity profile family for compressible turbulent boundary layers. *AIAA J* 31(9):1600–1604
- Humble RA (2009) Unsteady flow organization of a shock wave/boundary-layer interaction. Ph.D. thesis, Delft University of Technology
- Kuntz DW, Amatucci VA, Addy AL (1987) Turbulent boundary-layer properties downstream of the shock-wave/boundary-layer interaction. *AIAA J* 25(5):668–675
- Liu K, Zhang K (2011) Experiment of dynamic angle-of-attack on a side wall compression scramjet inlet at Mach 3.85. In: 17th AIAA international space planes and hypersonic systems and technologies conference, AIAA 2011-2348
- Moeckel WE (1949) Approximate method for predicting form and location of detached shock waves ahead of plane or axially symmetric bodies. NACA TN 1921
- Muck K, Bogdonoff S, Dussauge JP (1985) Structure of the wall pressure fluctuations in a shock-induced separated turbulent flow. In: 23rd aerospace sciences meeting, p 179
- Park SO, Chung Y, Sung HJ (1994) Numerical study of unsteady supersonic compression ramp flows. *AIAA J* 32(1):216–218
- Park SO, Lee C, Kang K (2001) Navier–Stokes analysis of a supersonic flow over moving compression ramp. In: 39th Aerospace sciences meeting and exhibit, p 568
- Pasquariello V, Hickel S, Adams N, Hammerl G, Wall W, Daub D, Willems S, Gülhan A (2015) Coupled simulation of shock-wave/turbulent boundary-layer interaction over a flexible panel. In: 6th European conference for aerospace sciences

- Piponniau S (2009) Instationnarités dans les décollements compressibles: cas des couches limites soumises à ondes de choc. Ph.D. thesis, Université de Provence
- Poggie J, Smits A (2001) Shock unsteadiness in a reattaching shear layer. *J Fluid Mech* 429:155–185
- Roberts TP (1989) Dynamic effects of hypersonic separated flow. Ph.D. thesis, University of Southampton
- Schülein E (2006) Skin friction and heat flux measurements in shock/boundary layer interaction flows. *AIAA J* 44(8):1732–1741
- Schülein E, Wagner A (2015) Freestream disturbance characterization in DNW-RWG at Mach 3 and 6. DLR 224 2014 C 169
- Schülein E, Krogmann P, Stanewsky E (1996) Documentation of two-dimensional impinging shock/turbulent boundary layer interaction flow. DLR Report DLR IB 223-96 A 49
- Selig MS, Andreopoulos J, Muck KC, Dussauge JP, Smits AJ (1989) Turbulence structure in a shock wave/turbulent boundary-layer interaction. *AIAA J* 27(7):862–869
- Settles GS, Bogdonoff SM, Vas IE (1976) Incipient separation of a supersonic turbulent boundary layer at high Reynolds numbers. *AIAA J* 14(1):50–56
- Settles GS, Perkins J, Bogdonoff S (1981) Upstream influence scaling of 2d and 3d shock/turbulent boundary layer interactions at compression corners. In: 19th aerospace sciences meeting, p 334
- Souverein LJ (2010) On the scaling and unsteadiness of shock induced separation. Ph.D. thesis, Delft University of Technology
- Souverein L, Bakker P, Dupont P (2013) A scaling analysis for turbulent shock-wave/boundary-layer interactions. *J Fluid Mech* 714:505–535
- Thomke G, Roshko A (1969) Incipient separation of a turbulent boundary layer at high Reynolds number in two-dimensional supersonic flow over a compression corner. NASA CR 73308
- Zheltovodov A, Schülein E, Horstman C (1993) Development of separation in the region where a shock interacts with a turbulent boundary layer perturbed by rarefaction waves. *J Appl Mech Tech Phys* 34(3):346–354
- Zukoski EE (1967) Turbulent boundary-layer separation in front of a forward-facing step. *AIAA J* 5(10):1746–1753

**Publisher's Note** Springer Nature remains neutral with regard to jurisdictional claims in published maps and institutional affiliations.